Annexe B

Microlensing in H1413+117 : disentangling line profile emission and absorption in a Broad Absorption Line quasar

B.1   Introduction

Dans cette annexe, nous fournissons l'article de Hutsemékers et al. [2009] dont nous sommes co-auteur. Cet article discute les observations spectroscopiques des composantes du mirage H1413+117 obtenues sur une période de seize années et couvrant le domaine UV/visible dans le référentiel du quasar. Ce quasar BAL montre en effet des différences spectrales dans les profils de raie P Cygni des composantes, la composante D semblant particulièrement affectée par un phénomène de microlentille gravitationnelle. Une partie des résultats publiés dans cet article ont été présentés dans le Chapitre 11.

Microlensing in H1413+117 : disentangling line profile emission and absorption in a Broad Absorption Line quasar[⋆]

D. Hutsemékers[1,⋆⋆], B. Borguet[1,⋆⋆⋆], D. Sluse[2], P. Riaud[1], and T. Anguita[2]

[1] Institut d'Astrophysique et de Géophysique, Université de Liège, Allée du 6 Août 17, B5c, B-4000 Liège, Belgium

[2] Astronomisches Rechen-Institut am Zentrum fuer Astronomie der Universitaet Heidelberg, Moenchhofstrasse 12-14, 69120 Heidelberg, Germany

ABSTRACT

On the basis of 16 years of spectroscopic observations of the four components of the gravitationally lensed Broad Absorption Line (BAL) quasar H1413+117, covering the ultraviolet to visible rest-frame spectral range, we analyze the spectral differences observed in the P Cygni-type line profiles and use the microlensing effect to derive new clues on the BAL profile formation. We first find that the absorption gradually decreases with time in all components and that this intrinsic variation is accompanied by a decrease of the intensity of the emission. We confirm that the spectral differences observed in component D can be attributed to a microlensing effect lasting at least a decade. We show that microlensing magnifies the continuum source in image D, leaving the emission line region essentially unaffected. We interpret the differences seen in the absorption profiles of component D as due to an emission line superimposed onto a nearly black absorption profile. We also find that the continuum source is most likely de-magnified in component C, while components A and B are not affected by microlensing. Differential dust extinction is measured between the A and B lines of sight. We show that microlensing of the continuum source in component D has a chromatic dependence compatible with the thermal continuum emission of a Shakura-Sunyaev accretion disk. Using a simple decomposition method to separate the part of the line profiles affected by microlensing and coming from a compact region, from the part unaffected by this effect and ccming from a larger region, we disentangle the true absorption line profiles from the true emission line profiles. The extracted emission line profiles appear double-peaked suggesting that the emission is occulted by a strong absorber, narrower in velocity than the full absorption profile, and emitting little by itself. We propose that the outflow around H1413+117 is constituted of a high-velocity polar flow and a denser, lower-velocity disk seen nearly edge-on. Finally, we report on the first ground-based polarimetric mesurements of the four components of H1413+117.

Key words. Gravitational lensing – Quasars: general – Quasars: absorption lines –Quasars: individual : H1413+117

1. Introduction

The broad absorption lines (BALs) observed in the spectra of quasars (or QSOs, Quasi-Stellar Objects), blueshifted with respect to the broad emission lines (BELs), reveal the existence of massive, high-velocity outflows in active galactic nuclei (AGN). Such powerful winds can strongly affect the formation and evolution of the host galaxy, enrich the intergalactic medium, and regulate the formation of the large-scale structures (e.g. Silk and Rees 1998, Furlanetto and Loeb 2001, Scannapieco and Oh 2004, Scannapieco et al. 2005).

About 15% of quasars have BALs in their spectra (Reichard et al. 2003). Outflows may be present in all quasars if the wind is confined into a small solid angle so that BALs are only observed when the flow appears along the line of sight (Weymann et al. 1991). On the other hand, BAL QSOs could be quasars in an early evolutionary stage, washing out their cocoons (Voit et al. 1993, Becker et al. 2000).

Despite of many high-quality observational studies, in particular from spectropolarimetry (Ogle et al. 1999), no clear view of the geometry and kinematics of the BAL phenomenon has emerged yet. While pure spherically symmetric winds appeared too simple to account for the variety of observations (Hamann et al. 1993, Ogle et al. 1999), equatorial disks, rotating winds, polar flows, or combinations thereof, have been proposed with more or less success to interpret the observations of individual objects or small groups of them (e.g. Murray et al. 1995, Schmidt and Hines 1999, Lamy and Hutsemékers 2004, Zhou et al. 2006). Given the large parameter space characterizing non spherically symmetric winds, BAL profile modeling must then be combined with other techniques to determine the outflow properties in individual objects (e.g. Young et al. 2007).

An interesting method which can bring independent information on the quasar internal regions is the use of gravitational microlensing. Indeed, in a typical gravitationally lensed quasar, a solar mass star belonging to the lensing galaxy has an Einstein radius R_E (the microlensing cross section) of the order of 10^{-2} pc, which is is comparable to the size of the continuum source. The microlens, moving across the quasar core in projection, can successively magnify regions of area $\simeq \pi R_E^2$, inducing spectroscopic variations which could be used to extract information on the quasar structure (Schneider et al. 1992, and references therein). Several studies, based on simulations, have demonstrated the interest of microlensing analyses for under-

---

standing BAL QSOs (Hutsemékers et al. 1994, Lewis and Belle 1998, Belle and Lewis 2000, Chelouche 2005).

H1413+117 is a BAL QSO of redshift $z \simeq 2.55$ showing typical P Cygni-type profiles, i.e. profiles where the absorption is not detached from the emission. Turnshek et al. (1988) discussed the spectrum of H1413+117 in details and made the first attempts to disentangle the emission from the absorption assuming an intrinsic blue/red symmetry of the emission lines. H1413+117 is also a gravitationally lensed quasar constituted of four images (Magain et al. 1988; see Fig. 1). Evidence for microlensing in component D has been suggested from both photometry and spectroscopy (Angonin et al. 1990, Østensen et al. 1997). In particular, Angonin et al. (1990) found that the equivalent width of the emission lines is systematically smaller in component D than observed in the other components, a result which can be interpreted by microlensing of the continuum source, the larger region at the origin of the emission lines being unaffected. This effect, which appeared to last at least a decade (Chae et al. 2001, Anguita et al. 2008), offers the possibility to separate the microlensed attenuated continuum (i.e. the absorption profile) from the true emission line profile, thus providing new clues on the formation of BAL profiles (Hutsemékers 1993, Hutsemékers et al. 1994).

In the present paper, we homogeneously analyse the spectra of the four components of H1413+117 obtained from 1989 to 2005. The spectra cover the ultraviolet to visible rest-frame spectral range. In Sect. 3, we show that the spectral differences observed between the images can be consistently attributed to microlensing despite of intrinsic variations. In Sect. 4, using a simple method, we separate the parts of the spectra affected and unaffected by microlensing, which basically corresponds to the attenuated continuum and the emission lines. From these results, we derive a consistent view of the macro- and microlensing in H1413+117 (Sect. 5). Finally, with the "pure" absorption and emission profiles in hand, we discuss the formation of the BAL profiles and the implications for the geometry and the kinematics of the outflow (Sect. 6).

2. Data collection

Spectra of the four components of H1413+117 were gathered from archived and published data. Table 1 summarizes the characteritics of the spectra obtained over a period of 16 years, with the date of observation, the spectral range and average resolving power $R = \lambda/\Delta\lambda$, and the instrument used.

The visible spectra secured in 1989 with the bidimensional spectrograph SILFID at the Canada-France-Hawaii Telescope (CFHT) are described in Angonin et al. (1990) and Hutsemékers (1993). These spectra were obtained under optimal seeing conditions (0.''6 FWHM). They provided the first spectroscopic evidence for microlensing in H1413+117.

A series of spectra were obtained in 1993-1994 with the Hubble Space Telescope (HST) feeding the Faint Object spectrograph (FOS). They cover the UV-visible spectral range (gratings G400H and G570H). These data are described in Monier et al. (1998). A second series of HST spectra, yet unpublished, were obtained in 2000 using the Space Telescope Imaging Spectrograph (STIS) and the G430L grating (principal investigator : E. Monier; proposal # 8127). All HST data were retrieved from the archive and reduced using standard procedures for long slit spectroscopy and prescriptions by Monier et al. (1998).

In 2005, visible spectra were obtained with the integral field unit of the Visible MultiObject Spectrograph (VIMOS) attached to the European Southern Observatory (ESO) Very Large
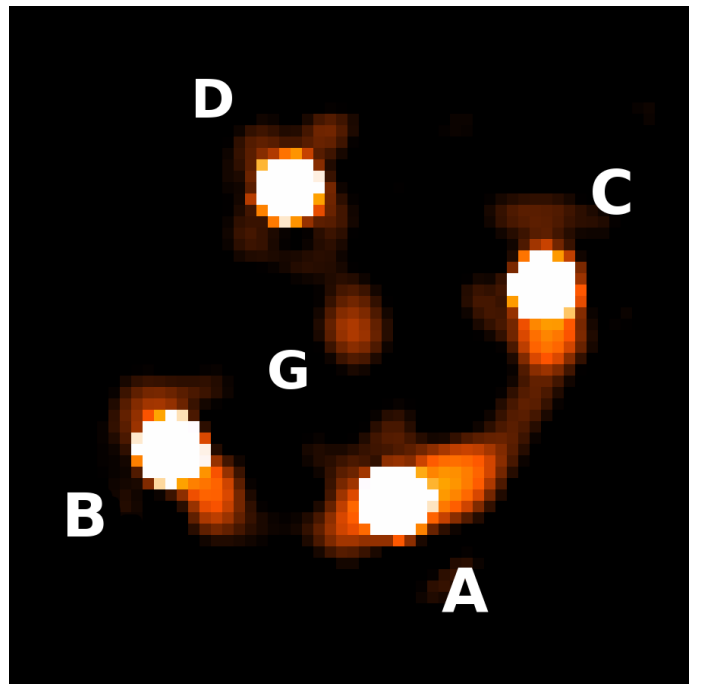

Fig. 1. A deconvolved near-infrared image of the gravitationally lensed quasar H1413+117 with the four images and the lensing galaxy labelled (from Chantry and Magain 2007). The image has been obtained in the F160W filter ($\lambda \simeq 1.6~\mu m$) with the NICMOS camera attached to the Hubble Space Telescope. North is up and East to the left. The angular separation between components A and D is 1.''1.

Telescope (VLT). The data were obtained under medium quality seeing conditions (1.''2 FWHM). Details on the observations and reductions are given in Anguita et al. (2008). For this data set, it was not possible to separate the spectra of images A and B of H1413+117.

The 2005 near-infrared spectra obtained with the integral field spectrograph SINFONI at the VLT were retrieved from the ESO archive (principal investigator : A. Verma ; proposal 075.B-0675(A)). Only the spectra obtained with the best seeing (0.''5 FWHM on May 22, 2005 in the H and K spectral bands) are considered here. The adopted pixel size was 0.''125×0.''250 on the sky. The observations consist of four exposures per spectral band. The object was positionned at different locations on the detector for sky subtraction. The data were reduced using the SINFONI pipeline. Telluric absorptions were corrected using standard star spectra normalized to a blackbody. The individual spectra were extracted by fitting a 4-gaussian function with fixed relative positions and identical widths to each image plane of the data cube using a modified MPFIT package (Markwardt 2009). Astrometric positions were taken from Chantry and Magain (2007). The spectra which appeared affected by detector defects and/or important cosmic ray hits were discarded. The good spectra were finally filtered to remove remaining spikes.

In addition, we have observed H1413+117 on May 10, 2008 with the polarimetric mode of the Focal Reducer and low dispersion Spectrograph 1 (FORS1) installed at the Cassegrain focus of the VLT. Observations have been carried out with the V_{high} filter, under excellent seeing conditions (0.''6).Linear polarimetry has been performed by inserting in the parallel beam a Wollaston prism, which splits the incoming light rays into two orthogonally polarized beams and a half- wave plate at four positions angles (e.g. Sluse et al. 2005). In order to measure the polarization of the four images, the MCS deconvolution procedure devised by

Table 1. Spectroscopic data

Date (y/m/d)	Spectral range	R	Instrument
1989/03/07	4400–6700 Å	~ 450	CFHT + SILFID
1993/06/23	4600–6800 Å	1300	HST + FOS
1994/12/24	3250–4800 Å	1300	HST + FOS
2000/04/21-26	3000–5700 Å	500–1000	HST + STIS
2005/03/18	3700–6700 Å	~ 250	VLT + VIMOS
2005/05/22	1.95–2.45 μm	~ 4000	VLT + SINFONI
2005/05/22	1.45–1.85 μm	~ 3000	VLT + SINFONI
2005/06/07	1.10–1.40 μm	~ 2000	VLT + SINFONI

Magain et al. (1998) has been applied. We used a version of the algorithm that allows for a simultaneous fit of different individual frames obtained with the same observational setup (Burud 2001). We constructed the PSF using a bright point-like object located ~ 15″ from H1413+117. Since this object is close to our target and is similar in brightness to the individual components of H1413+117, it provided a good estimate of the PSF. The Stokes parameters have been calculated from the photometry of the quasar lensed images derived from the deconvolution process.

3. Description of the spectra

At the redshift of H1413+117, spectra obtained in the UV-visible contain C IV $\lambda\lambda$1548,1550, Si IV $\lambda\lambda$1393,1402, N V $\lambda\lambda$1238,1242, P V $\lambda\lambda$1117,1128, O VI $\lambda\lambda$1031,1037, Lyα λ1216 and Lyβ λ1026, while the near-infrared spectra contain Hα λ6563, Hβ λ4861 and [O III] $\lambda\lambda$4959,5007 (Figs. 2 and 3). From the [O III] lines we measure the redshift z = 2.553. The UV resonance lines show typical P Cygni-type profiles with deep absorption while the Balmer lines show broad emission possibly topped with a narrower feature. Lyα and Lyβ lines are weak due to absorption by the N V and O VI ions, respectively (e.g. Surdej and Hutsemékers 1987).

3.1. Evidence for microlensing

In Figs. 2 and 3, we compare the profiles of various spectral lines observed in the different images A, B, C, and D of H1413+117. A scaling factor is applied to superimpose at best the continua, considering in particular the continuum windows 4525–4545 Å and 5165–5220 Å (i.e. 1275–1280 Å and 1450–1470 Å restframe, Kuraszkiewicz et al. 2002). If the four images are only macrolensed, the line profiles observed in the spectra of the four components must be identical up to the scaling factor. On the other hand, line profile differences between some components may be indicative of microlensing, which is expected to magnify the –small– continuum region and not the –larger– broad emission line region.

We first note that the line profiles in components A and B are essentially identical up to the scaling factor. This suggests that neither A nor B is strongly affected by microlensing. The difference observed in the [O III] lines is likely due to the spatial extension of the narrow line region (Chantry and Magain 2007). The wavelength dependence of the scaling factor reveals higher dust extinction along the B line of sight than along the A one, as discussed in details in Sect. 3.2. In the following we consider the average spectrum of components A and B, denoted AB, as the reference spectrum unaffected by microlensing effects. As seen

in the upper panel of Fig. 2, the spectrum of H1413+117 changes regularly with time, suggesting intrinsic variations in the quasar outflow (this is further discussed in Sect. 3.3). These changes are observed in all components, indicating that the time scale of the intrinsic line profile variation is longer than the time delays between the four images. The longest time delay is not larger than a few months according to the observations of Østensen et al. (1997), and possibly much smaller according to models[1] (Kayser et al. 1990, Chae and Turnshek 1999).

The spectrum of component D is clearly different when compared to AB. After scaling to the continuum, the emission in D appears less intense. This behavior is observed at all epochs and in the different spectral lines, superimposed onto the intrinsic time variations seen in all components. This is a clear signature of a long-term microlensing effect in D with amplification of the continuum with respect to the emission lines. The timescale of the effect is in agreement with previous estimates, i.e. of the order of 10 years (e.g. Hutsemékers 1993). As first pointed out by Angonin et al. (1990), a difference is also observed in the absorption profiles. This difference is especially strong in the 1989 and 1993 spectra. This is a priori not expected since the region at the origin of the observed absorption lines has the same spatial extent as the continuum source. Differential microlensing of an absorbing cloud smaller in projection than the continuum source has been proposed (Angonin et al. 1990). However the timescale of such an event is expected to be much smaller than 1 year (Hutsemékers 1993), ruling out this interpretation. Instead, we interpret this difference in the absorption profiles as due to the superposition of an emission line onto a nearly black absorption (Sect. 6.1).

Although not as strong as in component D, spectral differences are also observed when comparing C to AB. After scaling to the continuum, the emission lines in C appear slightly higher at all epochs. This suggests that microlensing also affects component C, de-amplifying the continuum with respect to the emission lines.

The scaling factor used to fit the continuum of D to that one of AB strongly depends on wavelength. This can be explained either by chromatic microlensing (the source of UV continuum is less extended than the source of visible continuum and then more magnified) or differential extinction (the extinction along the AB line of sight is higher than along the line of sight to D), or a combination of both. Such a strong wavelength dependence of the scaling factor is not observed when comparing C to AB. The origin of this effect is further discussed in Sect. 5.2.

3.2. The extinction curve from A/B

Since images A and B are not significantly affected by microlensing, the wavelength dependence of their flux ratio can be interpreted in terms of differential extinction in the lensing galaxy. Fig. 4 illustrates the observed flux ratio F_A/F_B using all available spectroscopic data (slightly filtered and smoothed). Photometric data are superimposed. They were collected from Angonin et al. (1990), Østensen et al. (1997; the ratios F_A/F_B are averaged per filter), Turnshek et al. (1997), Chae and Turnshek (2001), Kneib et al. (1998), Chantry and Magain (2007), MacLeod et al. (2009).

---

[1] We also estimate small time delays, typically less than 10 days, considering a classical singular isothermal ellipsoid (SIE)+shear model, a SIE+shear+galaxy model proposed by MacLeod et al. (2009), as well as using pixellated models with a symmetric mass distribution (Saha and Williams 2004).
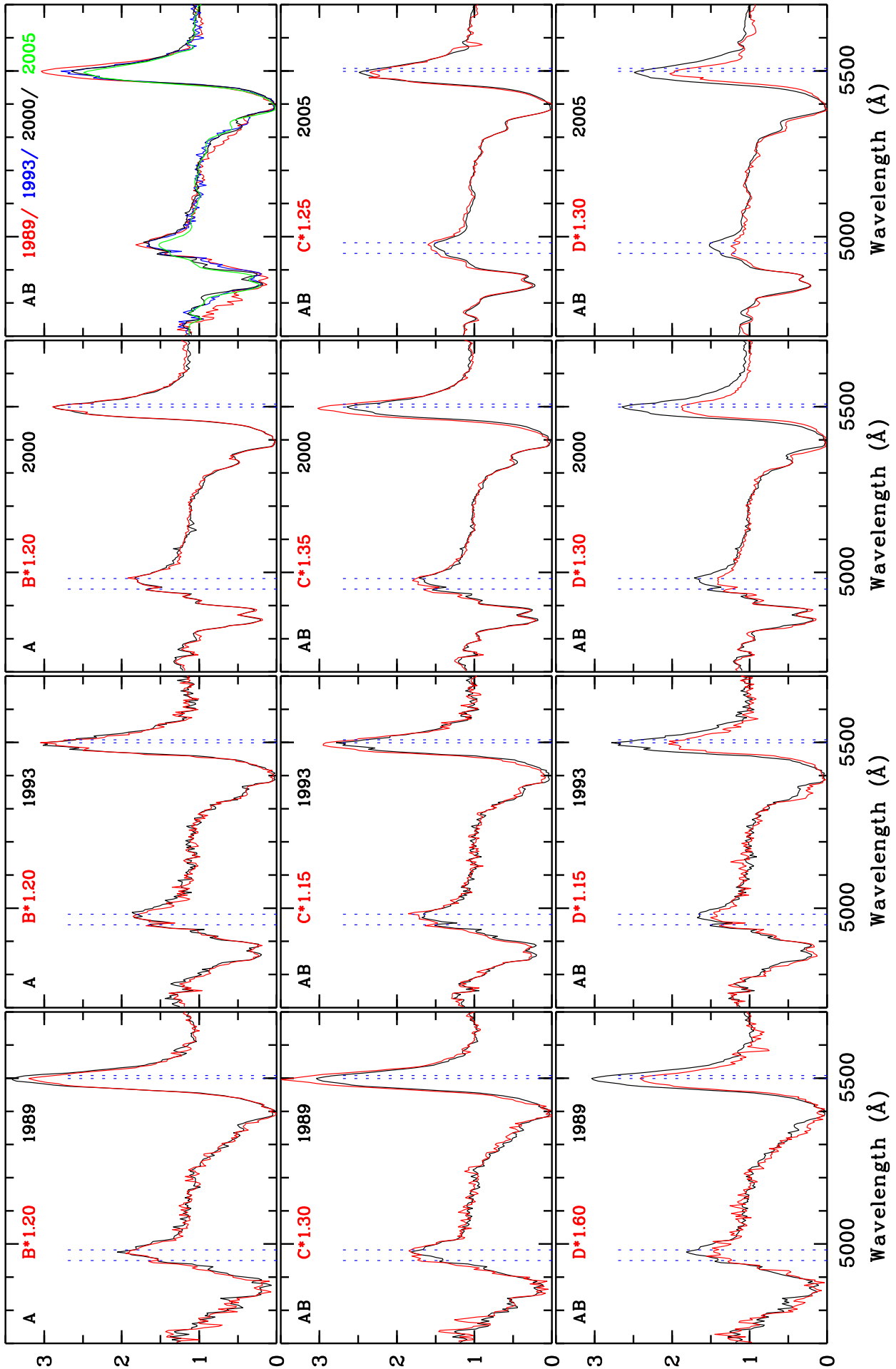
Fig. 2. Intercomparison, at different epochs, of the Si IV and C IV line profiles illustrating the spectral differences between some images of H1413+117. Ordinates are relative fluxes. Vertical dotted lines indicate the positions of the spectral lines at the redshift $z = 2.553$. The scaling factors needed to superimpose the continua are indicated. AB refers to the average spectrum of the A and B components (which could not be separated in the 2005 spectra). The upper left panel illustrates the time variation of the AB spectrum.
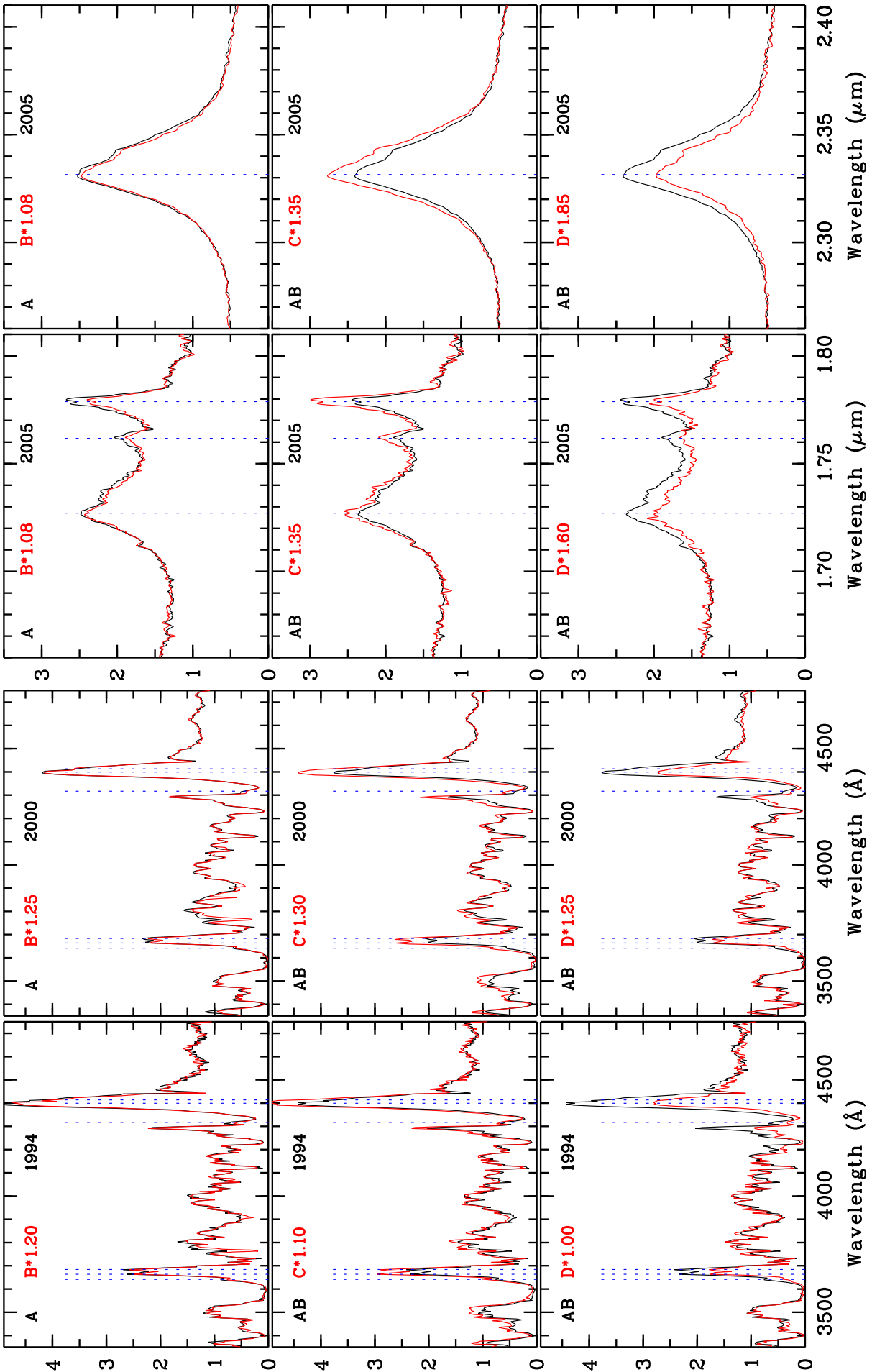
Fig. 3. Intercomparison of the Lyβ + O vi and Lyα + N v line profiles in the 4 images of H1413+117 at two epochs (lower panels). The comparison of the Hβ + [O iii] and Hα line profiles is shown in the upper panels. As in Fig. 2, ordinates are relative fluxes and vertical dotted lines indicate the redshifted line positions. The scaling factors needed to superimpose the continua are indicated.
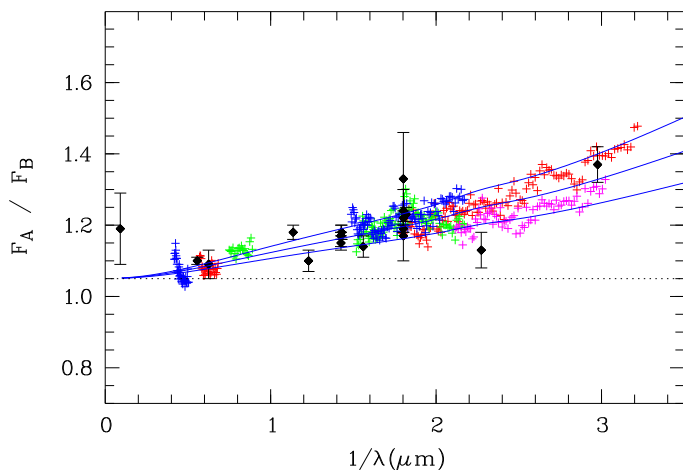
Fig. 4. The flux ratio F_A/F_B from the UV-visible spectra of 1989, 1993, 1994, 2000, and from the near-infrared spectra of 2005 (crosses of different colors). Photometric data point obtained at different epochs are superimposed (black diamonds with error bars). The continuous lines represent SMC-like extinction curves redshifted to $z_l = 1.0$.

There is a lot of dispersion in the measured flux ratios which arises not only from inacurracies in the data but also from a possible combined effect of intrinsic photometric variations and time delay (cf. Østensen et al. 1997). A clear trend is nevertheless observed, indicating higher extinction along the line of sight to image B, as suggested by Turnshek et al. (1997). The flux ratio is reasonably well fitted using

$$\frac{F_A}{F_B} = \frac{F_{A0}}{F_{B0}} \, 10^{-0.4\,\xi(\lambda)\,\Delta A_B} \tag{1}$$

where $\Delta A_B = A_B(A) - A_B(B)$ is the difference of extinction between the A and B line of sights measured in the B filter and $\xi(\lambda)$ the extinction curve tabulated in Pei (1992), redshifted to the redshift of the lens $z_l \simeq 1.0$ (Kneib et al. 1998). Since no obvious 2200Å feature typical of the Milky Way extinction is observed at 2.3 μm^{-1}, we adopt a SMC-like extinction curve. A reasonably good fit is obtained with $F_{A0}/F_{B0} = 1.05\pm0.02$ and $\Delta A_B = -0.09\pm0.02$ (Fig. 4). The flux ratio $F_{A0}/F_{B0} = 1.19\pm0.10$ measured by MacLeod et al. (2009) at 11 μm in the mid-infrared, i.e. at wavelengths were both extinction and microlensing are expected to be negligible, is compatible with the extinction corrected flux ratio F_{A0}/F_{B0} we derived, although marginally higher.

3.3. Intrinsic line profile variations

Time variations in the absorption line profiles of BAL quasars are not uncommon (Barlow et al. 1989, 1992, Gibson et al. 2008). In H1413+117, Turnshek et al. (1988) reported a deepening of the Si IV BAL between 1981 and 1985. Between 1989 and 2005 (Fig. 2), variations are observed as a gradual decrease of the strength of the BAL high-velocity component, the deepest low-velocity part of the profile being essentially unaffected. The strongest change occurs between 1989 and 1993 and corresponds to an increase of the luminosity (Remy et al. 1996, Østensen et al. 1997). Moreover, stronger absorption is accompanied by stronger emission, which is an indication that resonance line scattering can play an important role in the emission line formation. In the C IV line of the AB spectrum, the high-velocity absorption appears ~15% larger in 1989 than in 2005 while the emission is ~25% more intense. In the framework of

resonance scattering, where each absorbed photon is re-emitted, this suggests that the high-velocity outflow has more scattering material perpendicular to the line of sight than absorbing material along the line of sight, which also requires a large covering factor.

4. Decomposition of the line profiles

4.1. The method

We follow the method used in Sluse et al. (2007). Assuming that the observed spectra F_i are made of a superposition of a spectrum F_M which is only macrolensed and of a spectrum $F_{M\mu}$ which is both macro- and microlensed, it is possible to extract the components F_M and $F_{M\mu}$ by using pairs of observed spectra, if the relative macro-amplification M can be estimated.

Indeed, defining $M = M_1/M_2$ and $\mu = \mu_1/\mu_2$ as the macro- and micro-amplification ratios between image 1 and image 2, we have:

$$F_1 = MF_M + M\mu F_{M\mu} \tag{2}$$
$$F_2 = F_M + F_{M\mu} \, . \tag{3}$$

The latter equations can be rewritten to extract F_M and $F_{M\mu}$:

$$F_M = \frac{F_1/M - \mu F_2}{1 - \mu} \tag{4}$$
$$F_{M\mu} = \frac{F_2 - F_1/M}{1 - \mu} \, , \tag{5}$$

where M and μ must be chosen to satisfy the positivity constraints $F_M > 0$ and $F_{M\mu} > 0$. As demonstrated in Sluse et al. (2007), for a given M the only possible choice for μ is the value closest to $\mu = 1$ satisfying the positivity constraint $F_M > 0$ (Eq. 4).

The previous decomposition is exact when μ is constant as a function of wavelength, i.e. when the microlensing ratio is achromatic. This is reasonable as far as line profiles, which span small wavelength ranges, are considered. μ can nevertheless be different at different wavelengths, since the micro-amplification is related to the effective size of the magnified region which can be wavelength-dependent. Similarly, the macro-amplification factor M used in Eqs. 4 and 5 may contain a wavelength-dependent contribution due to differential extinction in the lensing galaxy, since extinction, like macrolensing, acts on the line profile as a whole. Finally, M is expected to remain identical at the different epochs of observation while μ can be time dependent.

4.2. The results

We extract the parts F_M and $F_{M\mu}$ from the spectra of H1413+117 using $F_1 = F_D$ and $F_2 = F_{AB}$ in Eqs. 4 and 5. We have $M < 1$ and $\mu > 1$ since D is fainter than AB and its continuum amplified (Sect. 3.1). Because $F_{M\mu}$ only depends on M up to a scaling factor, we first determine $F_{M\mu}$ by varying M in Eq. 5. Assuming that the major part of the emission lines is formed in a region much larger than the Einstein radius of the microlens and then essentially unaffected by microlensing, M is chosen as the value which leaves as little emission as possible in $F_{M\mu}$ over the wavelength range of a given line profile. For the UV-visible spectra, emission appears superimposed to a quasi-black absorption so that we adopt the largest $M < 1$ satisfying $F_{M\mu} > 0$. Smaller values of the macro-amplification factor M are possible but not

meaningful. Indeed, in such a case, an increase of the contribution due to micro-amplification will be needed to compensate for the low M. For the near-infrared spectra, we adopt the largest M which gives $F_{M\mu}$ with no depression at the position of the emission lines, i.e., as far as possible, a flat continuum-like spectrum. Then, we estimate F_M by varying μ in Eq. 4, adopting the smallest value of $\mu > 1$ which verifies the positivity constraint $F_M > 0$. The factor $(\mu M)^{-1}$ should be close to the scaling factor used in Figs. 2 and 3. The results of the line profile decomposition are given in Figs. 5 to 7.

Fig. 5 illustrates the spectral decomposition for the Si IV – C IV region. M was forced to be identical at all epochs. Values of M between 0.39 and 0.45 were found acceptable, the small values being more adequate for the 1989 data –which are the noisiest– while higher values (up to $M \simeq 0.45$) are acceptable for the post-1989 data. We adopt $M = 0.42$, noting that varying M between 0.39 and 0.45 does not significantly change the extracted spectra F_M and $F_{M\mu}$. Decreasing M below the adopted value will transfer emission from F_M to $F_{M\mu}$ which is not meaningful.

Although different values of μ were adopted at different epochs, the extracted spectra are remarkably consistent: the microlensed part of the spectrum, $F_{M\mu}$, contains the continuum, the full absorption line as well as a small contribution from the emission part of the profile, while the bulk of the emission lines appears in the macrolensed-only part of the spectrum F_M clearly showing a two-peak structure in C IV (at 5350 Å and 5500 Å). As F_M is the part of the emission not affected by microlensing, it shows the flux emitted from a large region of the quasar (much larger than the Einstein radius of the microlens), whereas $F_{M\mu}$ shows the flux emitted from a smaller region (comparable to and smaller than the Einstein radius). Just like the emission profiles seen in F_M are mostly coming from a large region, the absorption profiles seen in $F_{M\mu}$ are due to absorption affecting mostly (almost exclusively) the emission coming from the more compact region at the origin of the continuum. It is interesting to note that in our best quality spectrum (obtained in 2000), a faint continuum is seen between Si IV and C IV in F_M, i.e. not microlensed. Since no lines are expected in this spectral region (Kuraszkiewicz et al. 2002), this possibly supports the existence of an extended, scattered continuum in H1413+117, as suggested by polarization measurements (e.g. Lamy and Hutsemékers 2004).

The rest-frame UV spectra, and more particularly the Lyα + N V region were similarly analyzed (Fig. 6). Although the decomposition is less accurate due to structures in the continuum blueward of Lyα (possibly due to narrow absorption features and inaccuracies in the wavelength calibration), the extracted spectra $F_{M\mu}$ and F_M show the same qualitative behavior as observed in the C IV and Si IV line profiles.

Fig. 7 shows the decomposition for the Hβ + [O III] and Hα line profiles. M was choosen to have $F_{M\mu}$ as flat as possible with no depression at the position of the emission lines. The microlensed spectrum is clearly a flat continuum in the Hβ + [O III] spectral region, while there is weak evidence that a part of the Hα emission line region is microlensed in addition to the continuum source.

In principle, the same analysis can be done using the pair (C,AB). However the profile differences are weaker so that the extracted spectra are much noisier, μ being closer to 1 in Eqs. 4 and 5. Only the best spectra, extracted from the 2000 data which show the strongest profile differences (Figs. 2 and 3), are illustrated in Fig. 8. The resulting F_M and $F_{M\mu}$ are quite simi-

lar to those derived from the pair (D,AB). They require macro-amplification with $M \simeq 1$ and a de-magnification of the C continuum. From the near-infrared spectra, a flat $F_{M\mu}$ is obtained at the position of Hα with $M \simeq 0.88$. This value should be seen as a lower limit since a part of the Hα emission might be affected by microlensing as in component D. We then estimate $0.88 \leq M \leq 0.92$ and $\mu \simeq 0.8$ at the wavelength of Hα.

5. Lensing in H1413+117

5.1. The macro-amplification factors

In principle, the variation of M with wavelength can be attributed to differential extinction. Unfortunately, for the (D,AB) pair, the wavelength dependence is not clear enough to extract an extinction curve, given the uncertainties on the determination of M (Figs. 5 to 7). The results nevertheless suggest that the differential extinction between the AB and D lines of sight is smaller than between the A and B lines of sight for which the extinction at Lyα is ~ 1.2 times the extinction at Hα (Fig. 4). As a consequence, the value M(D,AB) = 0.40±0.01 determined at the wavelength of Hα should not differ from the true macro-amplification factor by more than 2%.

For the (C,AB) pair, we estimated $0.88 \leq M$(C,AB) ≤ 0.92 at the wavelength of Hα. M(C,AB) seems slightly wavelength dependent, providing (weak) evidence that extinction is smaller along the line of sight to C than along the line of sight to AB. Since the differential extinction remains small, we also assume that it does not affect this flux ratio by more than 2%.

The flux ratios with respect to component A are then $F_{B0}/F_{A0} = 0.95 \pm 0.02$ (Fig. 4), $F_{C0}/F_{A0} = 0.88 \pm 0.04$ and $F_{D0}/F_{A0} = 0.39 \pm 0.03$. The fact that F_{C0}/F_{A0} and F_{D0}/F_{A0} are different from the values estimated from photometry is due to a significant de-amplification of the C continuum and to a significant amplification of the D continuum, as derived from the analysis of the spectral lines. This emphasizes the need to properly correct for microlensing before interpreting the flux ratios.

Although only marginally different, the flux ratios of the B and C components relative to A seem slightly higher than the values $F_{B0}/F_{A0} = 0.84 \pm 0.07$ and $F_{C0}/F_{A0} = 0.72 \pm 0.07$ determined in the mid-infrared by MacLeod et al. (2009), i.e. where microlensing and extinction are thought to be negligible. If real, the origin of such a discrepancy is not clear but could be related to the intense starburst activity detected in the host galaxy of H1413+117 (Lutz et al. 2007, Bradford et al. 2009), which possibly contaminates the 11.2 μm (3.2 μm rest-frame) flux measurements with PAH emission.

5.2. Microlensing of the continuum source

The micro-amplification factor μ determined in component D depends on both the date and the wavelength (Figs. 5 to 7).

The strongest time variation of μ occurs between 1989 and 1993 (Figs. 2 and 5). It roughly corresponds to a relative photometric variation between A and D which can be observed in the V light curves of H1413+117 presented by Remy et al. (1996) and Østensen et al. (1997), superimposed onto the common intrinsic variation of the 4 components. Between 1993 and 2000, the variation of μ is weaker, in agreement with the HST photometry in the F555W filter reported by Turnshek et al. (1997) and Chae et al. (2001).

At a given epoch, μ decreases with increasing wavelength, suggesting chromatic magnification of the continuum source. This is best seen in the 2005 data (obtained within a 2 month
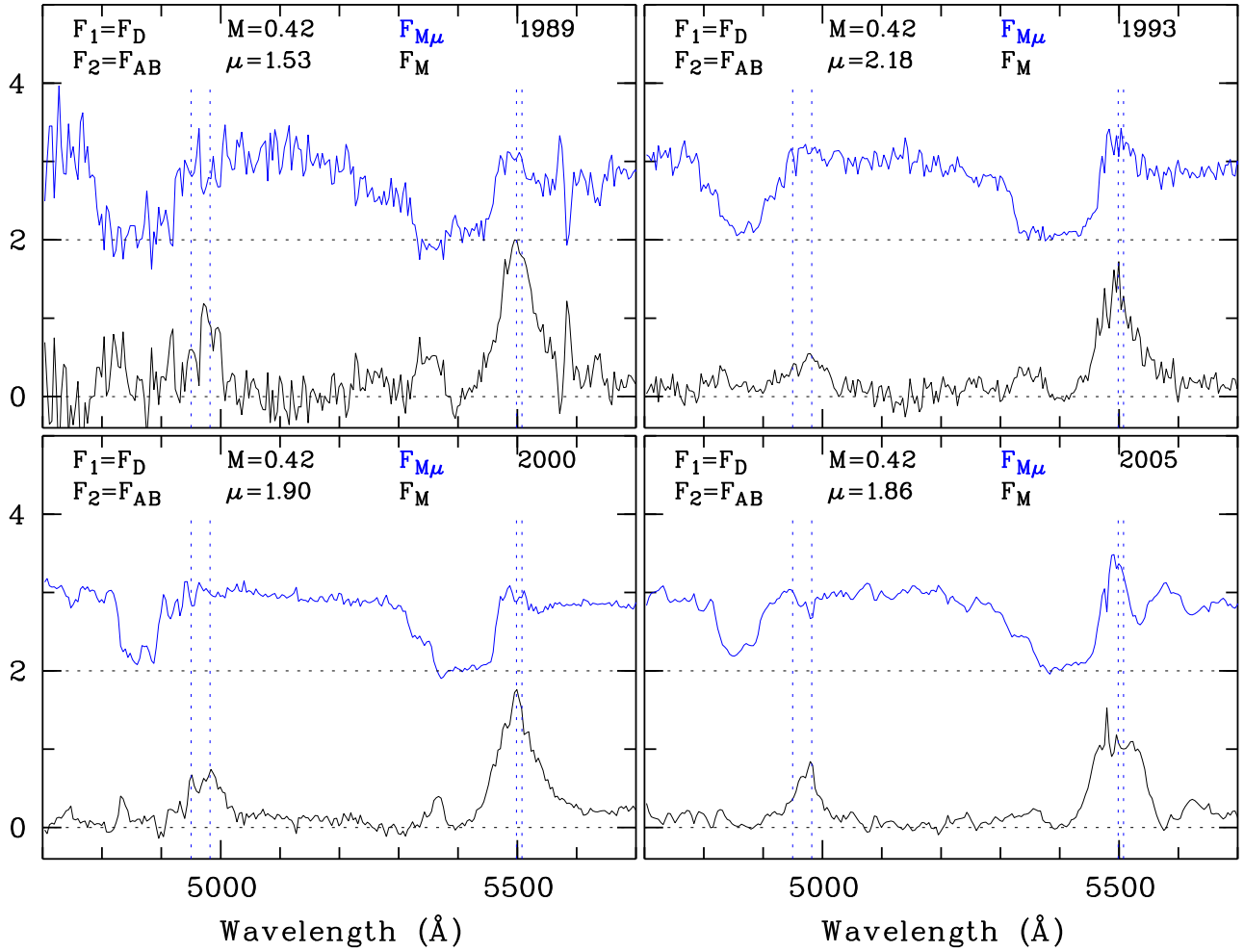
Fig. 5. The microlensed $F_{M\mu}$ and macrolensed-only F_M spectra of H1413+117 extracted from the comparison of the D and AB spectra, at different epochs.The Si IV and C IV line profiles are illustrated. The macro and micro-amplification factors M and μ are given for each epoch. Ordinates are relative fluxes, the $F_{M\mu}$ spectrum being shifted upwards by 2 units. Vertical dotted lines indicate the positions of the spectral lines at $z = 2.553$.
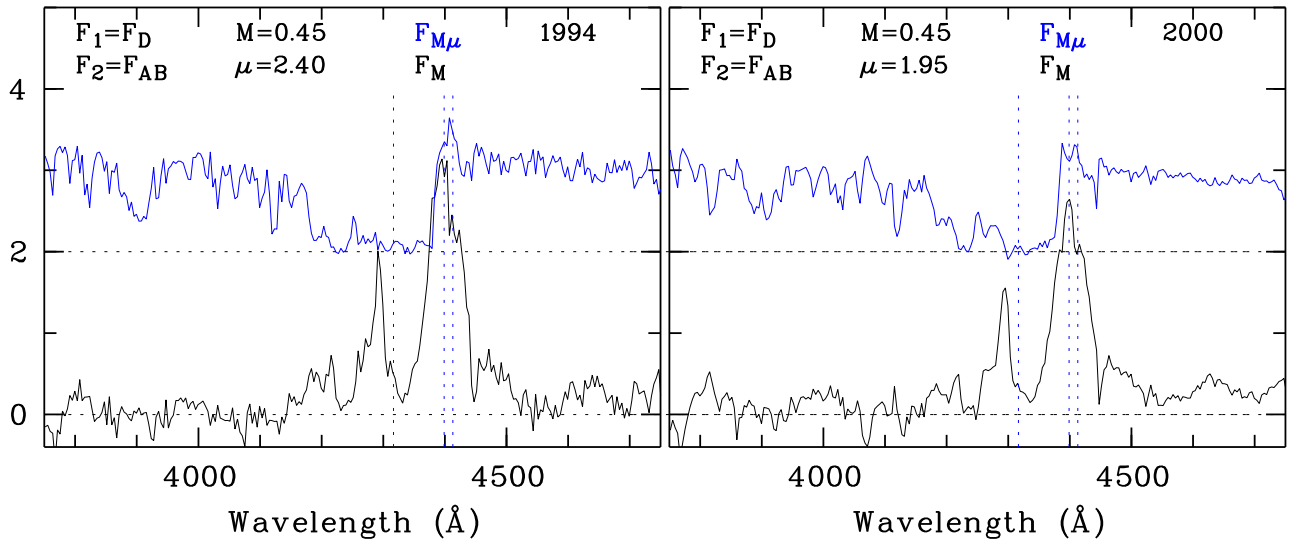

Fig. 6. Same as Fig. 5, but for the Lyα + N v line profile.

interval) which span the largest wavelength range. We emphasize that μ, when determined from the line profiles, is not contaminated by differential extinction (Sect. 4.1). In Fig. 9, we plot the values of μ determined in Figs. 5 and 7 as a function of the wavelength of observation in the quasar rest-frame.
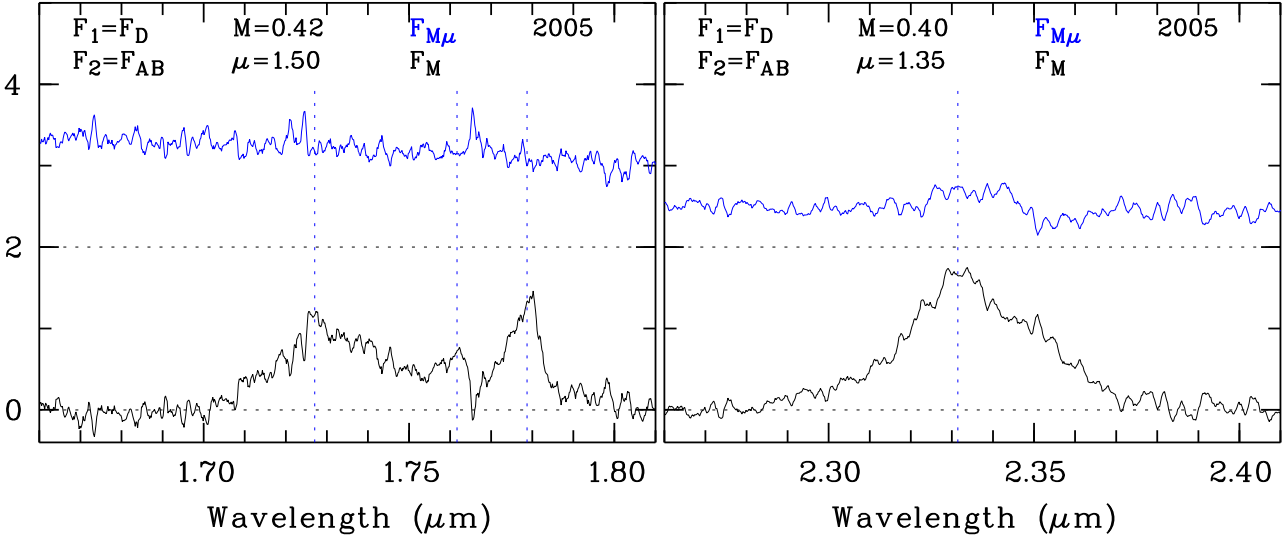
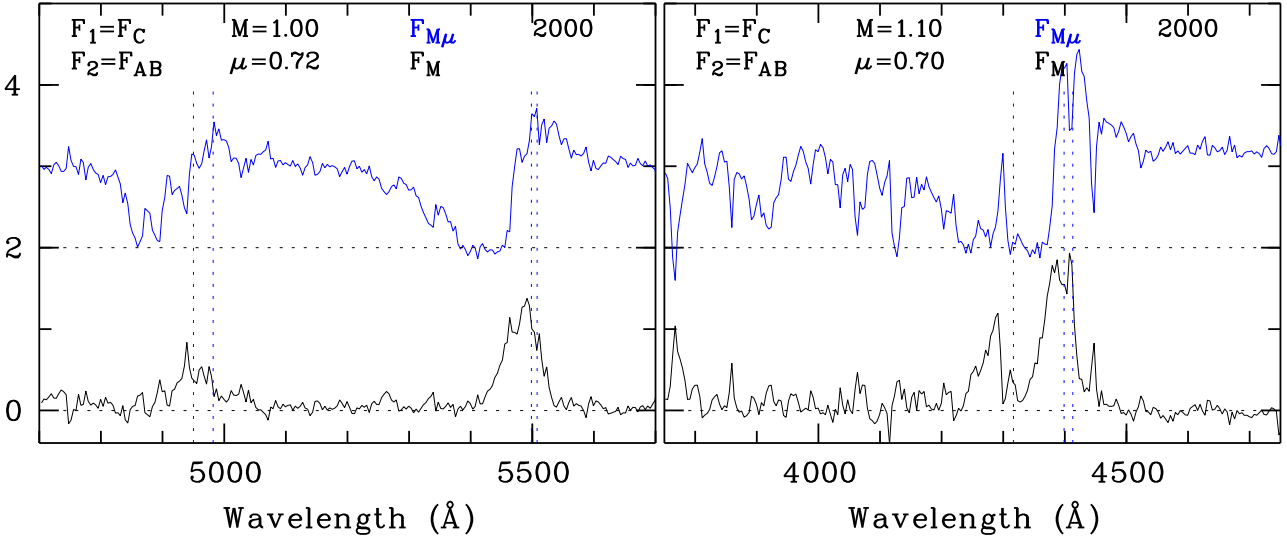**Fig. 7.** Same as Fig. 5, but for the Hβ + [O III] (left) and Hα (right) line profiles.

Fig. 8. Same as Fig. 5 and 6 but the microlensed $F_{M\mu}$ and macrolensed-only F_M spectra are extracted from the comparison of the C and AB spectra obtained in 2000. The Si IV and C IV (left) and Lyα + N V (right) line profiles are illustrated.

The magnification μ of an extended source close to a caustic can be written

$$\mu = \mu_0 + \frac{g}{\sqrt{R_S/R_E}} \zeta(d) \qquad (6)$$

where R_S is the source radius, R_E the Einstein radius of the microlens projected in the source plane, g is a constant of the order of unity, $\zeta(d)$ a function which depends on the distance to the caustic and μ_0 a constant "background" magnification (e.g. Schneider et al. 1992, Witt et al. 1993). In the framework a simple model where the continuum is emitted by a Shakura-Sunyaev (1973) thin accretion disk thermally radiating, $R_S(\lambda) \propto \lambda^{4/3}$ (e.g. Poindexter et al. 2008) such that we may expect

$$\log(\mu - \mu_0) = -\frac{2}{3}\log(\lambda) + C. \qquad (7)$$

As seen in Fig. 9, this model nicely reproduces the data using $C = -0.58$ and assuming for simplicity $\mu_0 = 1$ (i.e. no background (de-)magnification), supporting the idea of chromatic magnification of a continuum emitted by a Shakura-Sunyaev accretion disk.

In principle, we could have used the Lyα+N V and the C III] λ1909 emission lines, also present in the 2005 visible spectra, to measure μ at other wavelengths. Although tentative estimates do agree with the observed trend, the quality of the data is not sufficient to derive reliable estimates of μ at these wavelengths, due to the insufficient spectral resolution in the complex Lyα+N V region and to the fact that the C III] line is truncated. Clearly, with better quality data, it could be possible to separate M and μ at other wavelengths using additional line profiles and thus derive the brightness profile of the accretion disk.

From the value of the constant C, we can derive a rough estimate of the size of the continuum source : $R_S(\lambda)/R_E \lesssim \lambda^{4/3} 10^{2C}$. The Einstein radius is computed to be $R_E \simeq 0.01 \sqrt{M/M_\odot}$ pc using $z_l = 1.0$, a flat cosmology, $\Omega_m = 0.27$ and H$_0$ = 70 km s^{-1} Mpc^{-1}. M is the mass of the microlens. Finally, $R_S(\lambda) \lesssim 0.01 \sqrt{M/M_\odot}$ pc at the rest-frame UV wavelength $\lambda = 0.15$ μm. This radius agrees with the values obtained for the lensed quasars HE1104−1805 and Q2237+0305 on the basis of their photometric variability (e.g. Poindexter et al. 2008, Eigenbrod et al. 2008, Anguita et al. 2008b).
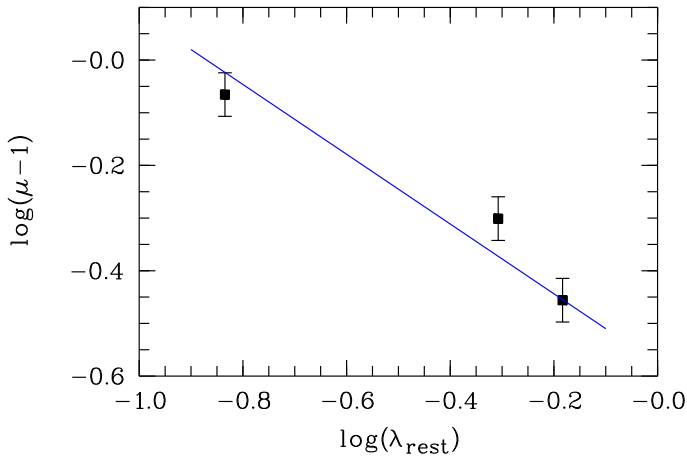
Fig. 9. The micro-amplification factor μ measured in 2005 (cf. Figs. 5 and 7) against the wavelength of observation expressed in the quasar rest-frame (in μm). A reasonable error of 10% on ($\mu - 1$) is shown. The straight line represents the model prediction (see text).

Table 2. Polarimetry of the four images

		A	B	C	D	ABC
p	1999/03	1.6±0.5	2.3±0.5	1.8±0.5	2.9±0.5	1.8±0.3
	1999/06	-	-	-	1.0±0.6	0.9±0.3
	2008/05	1.4±0.1	2.4±0.1	1.2±0.1	2.0±0.1	1.6±0.04
θ	1999/03	75±9	65±6	71±8	102±5	70±4
	1999/06	-	-	-	103±18	87±11
	2008/05	72±2	79±1	69±3	96±2	75±1

The polarization degree p is given in percent and the polarization position angle θ in degree. The data obtained in 1999 are from Chae et al. (2001).

5.3. Microlensing of a scattering region ?

Chae et al. (2001) have obtained the first polarization mesurements of the four images of H1413+117 using the HST. The F555W filter was used. They noted that, in March 1999, the polarization degree of component D might be higher that the polarization degree of the other components (Table 2). From this result, they suggested that microlensing also affects the scattering region. The measurements obtained in June 1999 possibly indicate an intrinsic variation of the polarization observed in all components. Similar variations have been reported by Goodrich and Miller (1995).

Taking advantage of an excellent seeing, we were able to measure the polarization of the 4 components of H1413+117 in the V filter, from the ground. Our measurements are also reported in Table 2. Within the uncertainties, the polarization degree of components A, B and C do agree with the March 1999 values of Chae et al. (2001), while the polarization degree of component D does not. Instead, we find that the difference between the polarization degrees measured in A and C and those ones measured in B and D is significant. The difference between A and B is especially intriguing since we found no significant microlensing effect neither in A nor in B (at least before 2005). Possible interpretations could involve the polarization due to an extended scattering region resolved by the macrolens (possibly in the host galaxy, see Borguet et al. 2008), or a differential polarization induced by aligned dust grains in the lens galaxy. More data are clearly needed to correctly understand the meaning of these measurements.

6. Consequences for the BAL formation

In the previous sections we derived a consistent picture of microlensing in H1413+117, showing that the continuum of component D (or more precisely all the regions of the quasar located in a cylinder of diameter $\sim 2\,R_E$ oriented along the line of sight and containing the continuum source) is magnified with respect to the more extended regions at the origin of the emission lines. This allowed us to disentangle the absorption part of the BAL profiles, essentially $F_{M\mu}$, from the emission part, essentially F_M (Figs. 5 to 7). The observed profiles are equal to the sum of the $F_{M\mu}$ and F_M spectra (Eq. 3). The separation is robust against the uncertainties of the macro-amplification factor M. It is however not perfect since emission which originates from regions close to the continuum source in projection will appear in $F_{M\mu}$. Selected spectra are illustrated in Fig. 10 on a velocity scale.

The absorption profile of the C IV BAL appears nearly black extending from $v \simeq -2000$ km s^{-1} to $v \simeq -10000$ km s^{-1}. It is especially interesting to note that the flow does not start at $v = 0$ in the rest-frame defined by the [O III] emission lines. The part of the profile between -8000 and -10000 km s^{-1} is clearly variable between 1993 and 2000, showing a smaller depth in 2000. The absorption appears stronger in N V and weaker in Si IV; this is best seen in the velocity range -2000 to -4000 km s^{-1} and indicates an ionization dependence of the optical depth.

The extracted emission profile shows a double-peaked structure which extends to the blue as far as the absorption profile does. The blue peak at -8000 km s^{-1} appears much fainter than the red peak at -1000 km s^{-1}. The full emission profile (represented by the green line in Fig. 10) is roughly centered on the onset velocity of the flow (-2000 km s^{-1}), thus blueshifted with respect to the [O III] rest-frame. In fact, the full absorption + emission line profile appears in a rest-frame blueshifted by -2000 km s^{-1} with respect the rest-frame defined by the [O III] emission lines. Hα, on the other hand, appears redshifted (Fig.3). Although not clearly understood, these line shifts are common in quasars (e.g. Corbin 1990, McIntosh et al. 1999) and particularly strong in BAL QSOs (Richards et al. 2002), in agreement with our observations.

The shape of the emission profile suggests that the emission is occulted by a strong absorber, narrower in velocity than the full absorption profile, and emitting little by itself. Very similar absorption and emission profiles are produced in the outflow model of Bjorkman et al. (1994) proposed for early-type stars. We build on this model to interpret our observations. A toy model, detailed in Appendix A, is used for illustrative purpose (a full radiative transfer modeling is beyond the scope of the present paper and left to a forthcoming work by Borguet and Hutsemékers, in preparation). We assume that the outflow in H1413+117 is constituted of two components: a quasi-spherically symmetric "polar" outflow, and a denser disk seen nearly edge-on. The disk is slower than the polar wind. The polar outflow produces typical P Cygni line profiles with a deep intrinsic absorption extending from -2000 to roughly -10000 km s^{-1} and a symmetric emission (assumed gaussian shaped for simplicity) of comparable equivalent width and due to resonantly scattered photons. This emission is centered on $v \simeq -2000$ km s^{-1} and extends from $+6000$ to -10000 km s^{-1}. Both the remaining unabsorbed continuum (if any) and the scattered emission are then absorbed in the slower disk for which we adopt the velocity and opacity laws needed to adequately reproduce the observations (Fig. 10). Little emission is expected from such an edge-on disk. As we can see from Fig. 10, this simple model is able to reproduce the gross characteristics of the emis-
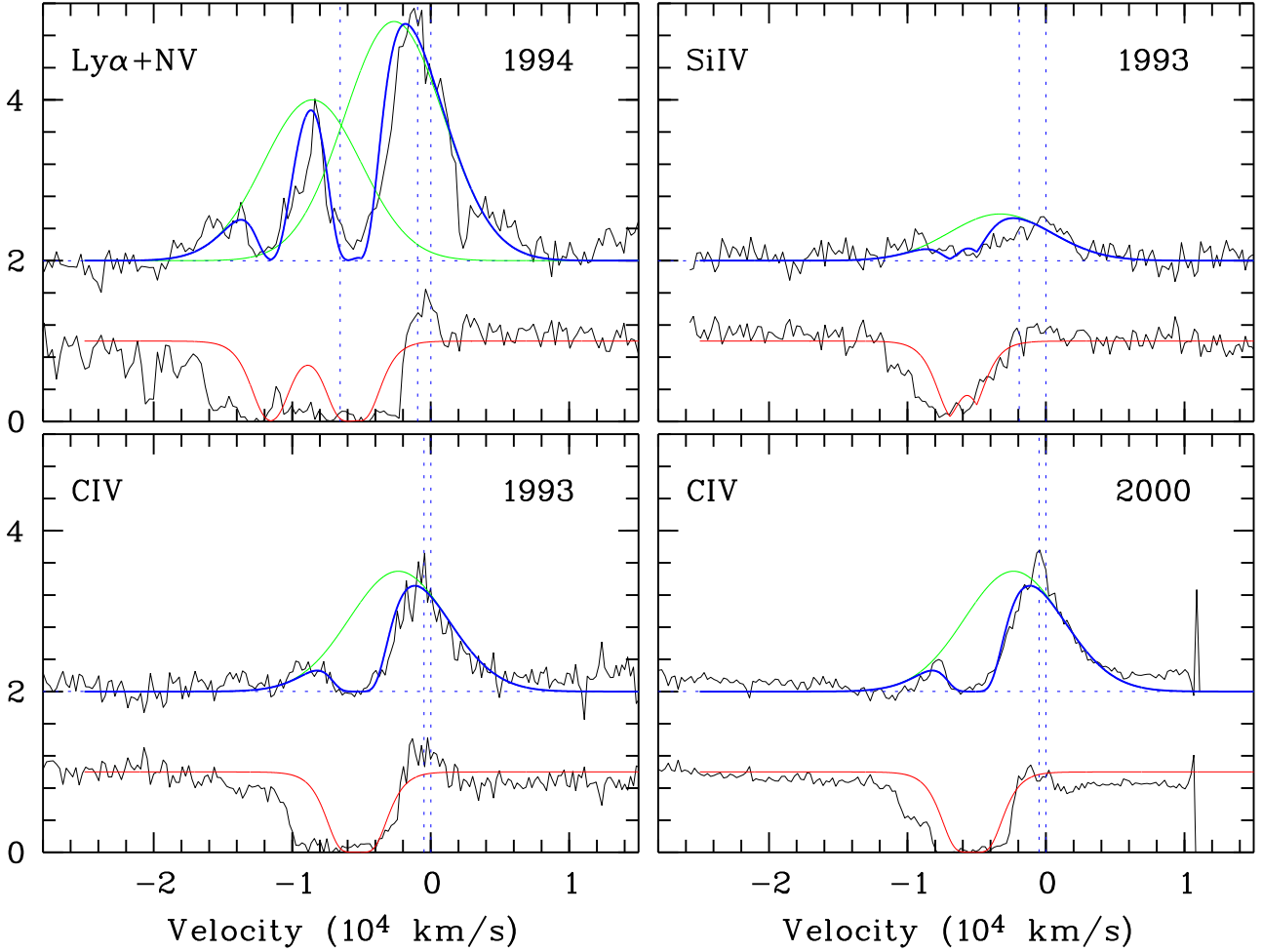
Fig. 10. Selected F_M and $F_{M\mu}$ spectra from Figs. 5 and 6 illustrated on a velocity scale. The zero velocity corresponds to the red line of the doublets redshifted using $z = 2.553$. Ordinates are relative fluxes. F_M is shifted upwards by 2 units. Vertical dotted lines indicate the positions of the spectral lines. The profiles from the model (Appendix A) are superimposed : the unabsorbed emission (green), the disk absorption profile (red) and the disk-absorbed emission (blue). The absorption in the polar flow is not modeled (see text).

sion line profiles. Variability of the polar flow optical depth will generate variations at the high velocity end of the absorption accompanied by a change in the resonantly scattered emission, as observed (Sect. 3.3; see also Bjorkman et al., 1994, for simulations). Note that two-component winds have good theoretical grounds (e.g. Murray et al. 1995, Proga and Kallman 2004) and are supported by many observations interpreted with either disks or polar flows (cf. Sect 1).

Spectropolarimetric observations of H1413+117 (e.g. Goodrich and Miller 1995, Lamy and Hutsemékers 2004) provide additional evidence favouring this kind of scenario. First, the polarization angle rotates within the absorption line profiles, suggesting the existence of at least two sources and/or mechanisms of polarization. The polar outflow and the disk, expected to produce perpendicular polarizations, can play this role, especially in the case of BAL QSOs with P Cygni-type profiles (Goodrich 1997, Hutsemékers et al. 1998, Lamy and Hutsemékers 2004). Furthermore, the absorption in the polarized spectrum is clearly narrower than the absorption in the direct spectrum (this is best observed in Fig. 3 of Goodrich and Miller, 1995), supporting the existence of a dense disk which absorbs the polar-scattered flux.

6.1. Microlensing in the BAL

The spectral difference seen between the high-velocity part of the BAL profiles of components AB and D (Fig. 2) can now be easily explained. In 1989 and 1993, the absorption at 5330 Å ($-9000 \, \mathrm{km \, s^{-1}}$) due to the polar outflow is nearly black, but filled in with emission resonantly scattered at the same velocity. Since the emission and the attenuated continuum react differently to the magnification by the microlens, a spectral difference is observed between AB and D. Later, in 2000 and 2005, this part of the flow is less optically thick: the absorption is not as deep as in the nineties and the resonantly scattered emission which fills in the absorption is accordingly weaker (the blue peak is narrower), with the consequence that the spectral difference between the AB and D BALs appears attenuated.

7. Conclusions

Using 16 years of spectroscopic observations of the 4 components of the gravitationally lensed BAL quasar H1413+117, we derived the following results.

− The strength of the BAL profiles gradually decreases with time in all components. This intrinsic variation is accompanied by a decrease of the intensity of the emission.

− The spectral differences observed in component D can be attributed to a stable microlensing effect, in agreement with previous studies. This effect consistently magnifies the continuum source of image D, leaving the BEL region essentially unaffected. We also find that the continuum of component C is most likely de-magnified, while components A and B are not affected by microlensing. Differential extinction is found between A and B.

− Using a simple decomposition method to separate the part of the line profiles affected by microlensing from the part unaffected by this effect, we were able to disentangle the intrinsic absorption (affected) from the emission line profile (unaffected). Consistent results are obtained for the different epochs of observation.

− Considering the macro- and micro-amplification factors estimated with this method, we obtain a coherent view of lensing in H1413+117. In particular, we show that microlensing of the D continuum source has a chromatic dependence which is compatible with a continuum emission by a Shakura-Sunyaev accretion disk.

− To interpret the extracted absorption and emission line profiles, we propose that the outflow from H1413+117 is constituted of a high-velocity polar flow (at the origin of the intrinsic variations) and a dense disk expanding at lower velocity and seen nearly edge-on. This is in agreement with spectropolarimetric data and supports the idea that BAL outflows can have large covering factors.

In our analysis, we focused on the most robust results. Several interesting questions nevertheless remain opened, requiring more observations or a full radiative transfer modeling. In particular, does the polarization of the different components actually differ, and why? Is the scattering region magnified or does it appear in the part of the spectrum unaffected by microlensing? High-quality spectropolarimetry of the four images of H1413+117 may solve this issue and bring more informations on the nature of the ouflow. As seen in Figs. 5 to 8, a small part of the emission lines appears microlensed, suggesting that this part of the emission arises close to the continuum source. More realistic line profile calculations are needed to understand the origin of this emission and what it tells us about the outflow kinematics. Finally, with excellent signal-to-noise spectra, it would be possible to also use the microlensing in the C component to derive complementary informations on the BAL region in H1413+117.

References

Angonin, M.-C., Vanderriest, C., Remy, M., Surdej, J. 1990, A&A, 233, L5
Anguita, T., Faure, C., Yonehara, A., Wambsganss, J., Kneib, J.-P., Covone, G., Alloin, D. 2008, A&A, 481, 615
Anguita, T., Schmidt, R. W., Turner, E. L., Wambsganss, J., Webster, R. L., Loomis, K. A., Long, D., McMillan, R. 2008, A&A, 480, 327
Barlow, T. A., Junkkarinen, V. T., Burbidge, E. M. 1989, ApJ, 347, 674
Barlow, T. A., Junkkarinen, V. T., Burbidge, E. M., Weymann, R. J., Morris, S. L., Korista, K. T. 1992, ApJ, 397, 81
Becker, R. H., White, R. L., Gregg, M. D., Brotherton, M. S., Laurent-Muehleisen, S. A., Arav, N. 2000, ApJ, 538, 72
Belle, K. E., Lewis, G. F. 2000, PASP, 112, 320
Bjorkman, J. E., Ignace, R., Tripp, T. M., Cassinelli, J. P. 1994, ApJ, 435, 416
Borguet, B., Hutsemékers, D., Letawe, G., Letawe, Y., Magain, P. 2008, A&A, 478, 321
Bradford, C. M., et al. 2009, arXiv:0908.1818
Burud, I. 2001, Ph.D. Thesis,
Chae, K.-H., Turnshek, D. A. 1999, ApJ, 514, 587
Chae, K.-H., Turnshek, D. A., Schulte-Ladbeck, R. E., Rao, S. M., Lupie, O. L. 2001, ApJ, 561, 653
Chantry, V., Magain, P. 2007, A&A, 470, 467
Chelouche, D. 2005, ApJ, 629, 667
Corbin, M. R. 1990, ApJ, 357, 346
Eigenbrod, A., Courbin, F., Meylan, G., Agol, E., Anguita, T., Schmidt, R. W., & Wambsganss, J. 2008, A&A, 490, 933
Furlanetto, S. R., Loeb, A. 2001, ApJ, 556, 619
Gibson, R. R., Brandt, W. N., Schneider, D. P., Gallagher, S. C. 2008, ApJ, 675, 985
Goodrich, R. W. 1997, ApJ, 474, 606
Goodrich, R. W., Miller, J. S. 1995, ApJ, 448, L73
Hamann, F., Korista, K. T., Morris, S. L. 1993, ApJ, 415, 541
Hutsemékers, D., Lamy, H., Remy, M. 1998, A&A, 340, 371
Hutsemékers, D. 1993, A&A, 280, 435
Hutsemékers, D., Surdej, J., van Drom, E. 1994, Ap&SS, 216, 361
Kayser, R., Surdej, J., Condon, J. J., Kellermann, K. I., Magain, P., Remy, M., Smette, A. 1990, ApJ, 364, 15
Kneib, J.-P., Alloin, D., Pello, R. 1998, A&A, 339, L65
Kuraszkiewicz, J. K., Green, P. J., Forster, K., Aldcroft, T. L., Evans, I. N., Koratkar, A. 2002, ApJS, 143, 257
Lamy, H., Hutsemékers, D. 2004, A&A, 427, 107
Lewis, G. F., Belle, K. E. 1998, MNRAS, 297, 69
Lutz, D., et al. 2007, ApJ, 661, L25
MacLeod, C. L., Kochanek, C. S., Agol, E. 2009, ApJ, 699, 1578
Magain, P., Surdej, J., Swings, J.-P., Borgeest, U., Kayser, R. 1988, Nature, 334, 325
Magain, P., Courbin, F., Sohy, S. 1998, ApJ, 494, 472
Markwardt, C. B. 2009, arXiv:0902.2850
McIntosh, D. H., Rix, H.-W., Rieke, M. J., Foltz, C. B. 1999, ApJ, 517, L73
Monier, E. M., Turnshek, D. A., Lupie, O. L. 1998, ApJ, 496, 177
Murray, N., Chiang, J., Grossman, S. A., Voit, G. M. 1995, ApJ, 451, 498
Ogle, P. M., Cohen, M. H., Miller, J. S., Tran, H. D., Goodrich, R. W., Martel, A. R. 1999, ApJS, 125, 1
Østensen, R., et al. 1997, A&AS, 126, 393
Pei, Y. C. 1992, ApJ, 395, 130
Poindexter, S., Morgan, N., Kochanek, C. S. 2008, ApJ, 673, 34
Proga, D., Kallman, T. R. 2004, ApJ, 616, 688
Reichard, T. A., et al. 2003, AJ, 126, 2594
Remy, M., Gosset, E., Hutsemékers, D., Revenaz, B., Surdej, J. 1996, Astrophysical Applications of Gravitational Lensing, 173, 261
Richards, G. T., Vanden Berk, D. E., Reichard, T. A., Hall, P. B., Schneider, D. P., SubbaRao, M., Thakar, A. R., York, D. G. 2002, AJ, 124, 1
Saha, P., Williams, L. L. R. 2004, AJ, 127, 2604
Scannapieco, E., Oh, S. P. 2004, ApJ, 608, 62
Scannapieco, E., Silk, J., Bouwens, R. 2005, ApJ, 635, L13
Schmidt, G. D., Hines, D. C. 1999, ApJ, 512, 125
Schneider, P., Ehlers, J., Falco, E. E. 1992, Gravitational Lenses, Springer-Verlag Berlin Heidelberg New York.
Shakura, N. I., Sunyaev, R. A. 1973, A&A, 24, 337
Silk, J., Rees, M. 1993, A&A, 331, L1
Sluse, D., Hutsemékers, D., Lamy, H., Cabanac, R., Quintana, H. 2005, A&A, 433, 757
Sluse, D., Claeskens, J.-F., Hutsemékers, D., Surdej, J. 2007, A&A, 468, 885
Surdej, J., Hutsemékers, D. 1987, A&A, 177, 42
Turnshek, D. A., Grillmair, C. J., Foltz, C. B., Weymann, R. J. 1988, ApJ, 325, 651
Turnshek, D. A., Lupie, O. L., Rao, S. M., Espey, B. R., Sirola, C. J. 1997, ApJ, 485, 100
Voit, G. M., Weymann, R. J., Korista, K. T. 1993, ApJ, 413, 95
Witt, H. J., Kayser, R., Refsdal, S. 1993, A&A, 268, 501
Weymann, R. J., Morris, S. L., Foltz, C. B., Hewett, P. C. 1991, ApJ, 373, 23
Young, S., Axon, D. J., Robinson, A., Hough, J. H., Smith, J. E. 2007, Nature, 450, 74
Zhou, H., Wang, T., Wang, H., Wang, J., Yuan, W., Lu, Y. 2006, ApJ, 639, 716

Appendix A: The absorption / emission toy model

For a given line profile, we adopt for the disk optical depth τ_d the functional form

$$\tau_d(w) = \sum_i \tau_0(i) \, \exp{-\left|\frac{w - w_{ca}(i)}{w_{sa}}\right|} \quad\quad (A.1)$$

where w is the velocity. $w_{ca}(i)$ is the position of the center of the absorption line i, and w_{sa} the width taken identical for all lines. The sum is computed over the 2 or 3 lines which constitute a line

profile, with the appropriate weights $\tau_0(i)$. Similarly, we adopt for the unabsorded emission line profile

$$f_e(w) = \sum_i f_{e0}(i) \ \exp - \left(\frac{w - w_{ce}(i)}{w_{se}} \right)^2 . \qquad (A.2)$$

The disk absorption profile is computed as $F_a = \exp(-\tau_d)$ and the emission line profile absorbed by the disk as $F_{ea} = f_e \exp(-\tau_d)$. The total absorption of the continuum is equal to the absorption by the polar flow (not modeled) multiplied by the absorption in the disk.

For all line profiles shown in Fig. 10, we use $w_{ca}(1) = -5000$ km s^{-1}, $w_{sa} = 800$ km s^{-1}, $w_{ce}(1) = -2000$ km s^{-1}, $w_{se} = 5000$ km s^{-1}, $i = 1$ corresponding to the reddest line of the profiles, the position of the other ones being fixed by the doublet separation and/or by the Lyα – N v velocity separation. The parameters $\tau_0(i)$ and $f_{e0}(i)$ are choosen to fit the observations.